

A three-dimensional numerical model for a convection–diffusion phase change process during laser melting of ceramic materials

J.F. Li ^{a,b,*}, L. Li ^a, F.H. Stott ^b

^a *Laser Processing Research Centre, Department of Mechanical, Aerospace and Manufacturing Engineering, University of Manchester Institute of Science and Technology (UMIST), P.O. Box 88, Manchester M60 1QD, UK*

^b *Corrosion and Protection Centre, UMIST, P.O. Box 88, Manchester M60 1QD, UK*

Received 23 March 2004

Available online 16 September 2004

Abstract

Using a fixed-grid source-based method, a three-dimensional numerical model for a convection–diffusion phase change process during laser melting of ceramic materials has been studied. The model was applied to a realistic binary phase diagram containing a eutectic composition, including both an isothermal phase change occurring at a distinct temperature and a phase change taking place over a temperature range (the “mushy” region phase change). The effects of latent heat of fusion and fluid flow in the melt pool on the temperature, velocity fields and shape of the melt pool were analysed and compared. Results indicated that the effects of latent heat of fusion were more significant than those of fluid flow for two simulation cases, considered in the model. The best prediction accuracy for the profiles of the melt/solid interfaces was achieved from the developed model by considering both the latent heat of fusion and fluid flow in the melt pool.

© 2004 Elsevier Ltd. All rights reserved.

Keywords: Laser; Melting; Ceramics; Marangoni flow; Phase change

1. Introduction

Laser surface melting of ceramic materials, such as architecture and refractory materials, for sealing relatively porous surfaces and/or achieving dense, homogeneous and corrosion-resistant surface layers, has drawn

increased interest over recent years [1–5]. A key aspect during such surface processing is to minimize the occurrence of cracks due to thermally-induced and/or residual stresses. These stresses are closely associated with thermal distribution, melting and solidification of the treated materials during processing, as well as the resulting microstructural features of the obtained surface layers. Relative to laser surface melting of metallic materials, much less fundamental understanding for laser melting of ceramic materials is apparent from the literature. Empirically, it was found that the extent of occurrence of cracks during laser surface treatment of ceramic materials was sensitive to the processing parameters

* Corresponding author. Address: Department of Mechanical, Aerospace and Manufacturing Engineering, Laser Processing Research Centre, Institute of Science and Technology (UMIST), University of Manchester, P.O. Box 88, Manchester M60 1QD, UK. Tel.: +44 161 200 3827; fax: +44 161 200 3803.
E-mail address: ljfwxxy@yahoo.com (J.F. Li).

for the melt cross-sections, formed under normal laser processing conditions, could be reasonably attributed to neglecting fluid flow caused by surface tension and buoyancy in the model. Therefore, more complicated computational models, using numerical approaches, e.g., the finite difference method or the finite element method, and taking into account of fluid flow are necessary for more accurate prediction of the thermal field.

Numerical models for investigation of thermal behaviour and fluid flow in the melt pool formed during laser processing of metallic materials have been well developed in the literature [6,9]. These models are mainly based on the “fixed-grid enthalpy-based” method [10]. By introducing scalar of liquid fraction and applying a source-based method, the unique continuity, momentum and energy equations can be solved for both liquid and solid phases; thereby, the major difficulty associated with a moving phase-change interface, across which certain jump conditions must be satisfied and whose location is an unknown priori, is overcome. In this method, the energy equation is generally written in terms of the sensible enthalpy, and an appropriate formulation of the latent heat function plays a pivotal role in assuring that the results from the energy equation are consistent with phase-change considerations. The most recent effort to solve this problem was by Chakraborty and Dutta [11], who outlined a generalized formulation for evaluation of latent heat functions that addressed a wide variety of phase-change situations. However, all the developed numerical methodologies have been applied to either isothermal phase changes occurring at a distinct temperature [12–14] or phase changes that take place over a temperature range (termed the “mushy” zone phase change) [10]. Under the situations where poor convergence occurs, various methods have been used to prevent numerical oscillations for the two types of phase change.

To date, to the authors’ knowledge, theoretical models for laser melting of ceramic materials have neglected fluid flow of the molten body [15,16]. The latent heats of fusion of ceramic materials are somewhat higher, and their thermal diffusivities and conductivities are generally one order of magnitude lower, than those of metallic materials. It can, hence, be predicted that the interlinkage between the coupled energy and momentum equations would lead to more significant numerical oscillations for the nodes around the phase-change interfaces, resulting in difficulty in convergence of calculation. In the present paper, a three-dimensional numerical model for the convection–diffusion phase change process during laser melting of ceramic materials has been studied. Compared with the models developed for laser melting of metallic materials [6,9], the present model has treated phase changes during melting of ceramics that include a eutectic composition, including the processes of both an isothermal phase change and

a phase change over a range of temperatures, respectively, and a moving volumetric heating source rather than a surface heating source. The computations of the flow and temperature were carried out using a fixed-grid, primitive-variable and control-volume based finite difference method, with a direct temperature–porosity formulation to treat melting and solidification. The permeability term [6], relating to the liquid volume fraction of every control volume, in the momentum equations, has been under-relaxed, with a relatively large relaxation factor of 0.9, to restrain the numerical oscillations during iteration. In addition, the resulting temperatures, velocity fields and shapes of the melt pool were compared with those obtained from corresponding numerical models of pure heat conduction and of heat conduction incorporating latent heat of fusion. The melt cross-section parameters, including melt depths, widths, areas and cross-sectional profiles predicted from these models, were also compared with experimental results.

2. Modelling of laser surface melting

2.1. Thermal model description

The laser surface melting of ceramic materials is briefly illustrated in Fig. 1. A continuous laser beam, of sufficient intensity, is incident upon a workpiece of the treated ceramic material, moving at a constant velocity. A significant fraction of the incident light energy is absorbed by the workpiece, and the very intensive heat flux under the laser beam leads to formation of a melt pool. This solidifies to produce a dense track. Treated surface layers having a large area can be accomplished by successive treatment passes with a certain overlapping ratio, for example, 50%, in the direction vertical to the direction of the moving workpiece. Previous experimental investigation [17] showed that the trends in terms of the effects of the process parameters: laser power and moving velocity of the workpiece, on the occurrence of cracks in the laser treated large-area

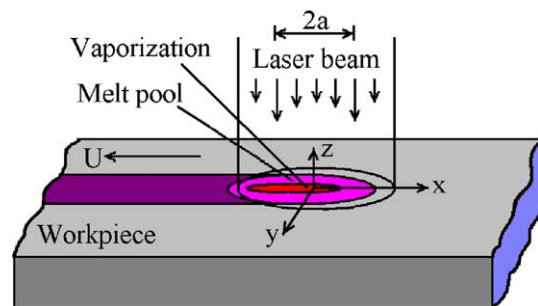


Fig. 1. Schematic diagram of the ceramic workpiece during laser surface melting.

surface layers were the same as those in the corresponding single treated tracks. Thus, in the present modelling procedure, a single laser treated track has been selected, for simplification. This is a typical problem of a convection–diffusion phase change process incorporating a moving heating source. The physical assumptions for the model are listed as follows:

(i) The model mainly considers the momentum and heat transport for the fully developed melt pool; thus, the field variables, including temperature and flow velocity, are considered to be quasi-steady. However, the final shape and size of the melt pool are closely dependent on their transient evolution [14]. Thus, the quasi-steady temperature and fluid fields for the fully developed melt pool are solved from the corresponding transient equations until they reach the steady values [18].

(ii) The treated workpiece has dimensions of 80 mm × 80 mm × 15 mm for the calculation. The methodology, used in Ref. [19] to describe a two-dimensional quasi-steady thermal model of laser cladding, has been employed to describe the present three-dimensional quasi-steady convection–diffusion phase change. The “downwind” boundary on the left, where both the treated track and the substrate leave the calculation domain, is taken as an adiabatic wall, while the boundary at which the workpiece material enters on the right side of the calculation domain is maintained at a constant temperature.

(iii) The latent heat of fusion is calculated from a non-linear temperature–composition relationship as occurs in a realistic phase diagram. The workpiece material used in the modelling procedure is a type of alumina-based refractory ceramic. It contains approximately 75% corundum, 24% mullite and 1% cristobalite by weight. Thus, the latent heat of fusion is calculated according to the binary SiO_2 – Al_2O_3 phase diagram, as shown in Fig. 2 [20]. Note that there is a mullite– Al_2O_3 eutectic composition at 78% Al_2O_3 by weight. The phase change at the melting and solidifying inter-

faces must include situations where phase changes occur both at a distinct temperature and over a temperature range.

(iv) The top surface of the melt pool is assumed to be flat. The flow in the melt pool is laminar and incompressible. Accurately, the top surface should be modelled as a free surface boundary that depends on the surface tension, gravity and vapour pressure. This assumption of a flat top surface of the melt pool simplifies the boundary condition, as in previous numerical models for fluid flow in melt pools of metallic materials formed by laser and other high energy density beams [6,9,14]. This approximation is quite reasonable because experimental results showed that the treated tracks of the refractory ceramic, used for the present modelling, were quite flat at the surfaces, under the normal laser melting parameters.

(v) Heat loss due to vaporization can be taken into consideration if a sufficiently intensive laser power is applied. In such a case, it is assumed to be continuous in the temperature between the vapour and the melt. The vapour behaves as an ideal gas and follows the Clausius/Clapeyron equation [21]. Vaporization is handled by giving the temperatures at the melt/vapour interface values equal to those determined as a function of the absorbed laser intensity [21].

(vi) The thermal properties of the refractory ceramic, such as specific heat and thermal conductivity, are isotropic, but temperature-dependent, as shown in Fig. 3 [3,22–25]. Here, the porosity of the refractory ceramic has been assumed to contribute to decreasing the values of thermal conductivity and thermal diffusivity [25]. Due to the lack of high-temperature data for the refractory ceramic chosen for this work, the dynamic viscosity and temperature coefficient of surface tension of the molten body are both taken as the values for liquid alumina [26,27]. Fig. 4 shows the dynamic viscosity, as a function of temperature. Except for those shown in Figs.

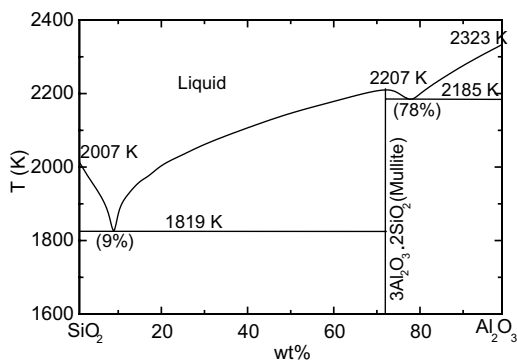


Fig. 2. The binary SiO_2 – Al_2O_3 phase diagram used to describe laser melting of the refractory ceramic [20].

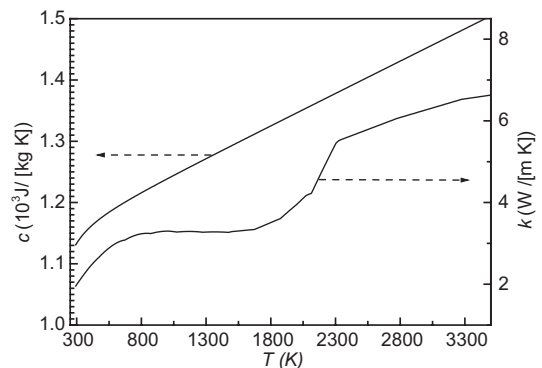


Fig. 3. Temperature-dependent specific heat and thermal conductivity for the workpiece ceramic used in the simulation [22–25].

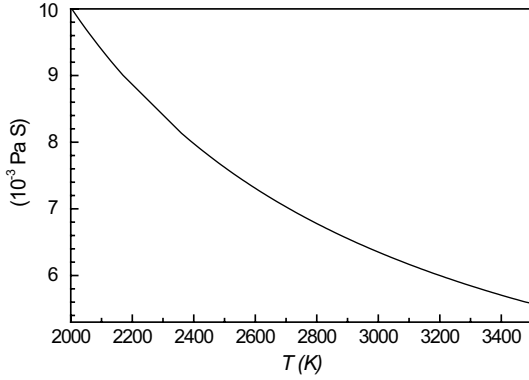


Fig. 4. Temperature-dependent dynamic viscosity for the workpiece ceramic used in the simulation [27].

Table 1
Temperature-independent physical properties of the refractory ceramic used for the simulation

Property	Value	Reference
r	0.15	[4,8]
T_{sol} (K)	2185	[3,20]
T_{liq} (K)	2243	[3,20]
$T_{vap,0}$ (K)	3253	[3,23,24]
L_V (kJ kg ⁻¹)	4102	[3,23,24]
β (K ⁻¹)	4×10^{-5}	[26,27]
ϵ	0.9	[23]
γ (μm)	345	[29]
ρ (kg m ⁻³)	3180	[4]
σ_T (N m ⁻¹ K ⁻¹)	6×10^{-5}	[26,27]

3 and 4, the other physical properties of the refractory ceramic are independent of temperature and are listed in Table 1.

(vii) The heating source is a mixture of the Gaussian and Doughnut modes, containing 35% of the former. There is no plasma formation. The vapour is transparent to the incident laser irradiation, and the reflectivity of the workpiece material is independent of temperature. The laser energy penetrating into the workpiece is expressed, as a volumetric heating source, by means of the Beer Lambert’s law [28,29].

2.2. Mathematical formulation

For the mathematical formulation, a Cartesian geometry is employed: the x - y plane of the coordinate system lies on the surface of the workpiece and the origin coincides with the centre of the laser beam. The workpiece moves in the negative x direction at a constant velocity U , and its right side of the calculation domain is 30mm from the origin. The laser beam modelling as a volumetric heating source can be expressed as [28,29]

$$q(x, y, z) = \frac{(1 - r)I(x, y)}{\gamma} \exp\left(-\frac{|z|}{\gamma}\right) \quad (1)$$

where $I(x, y)$ is the laser intensity at the top surface, if a mixture of the Gaussian and Doughnut modes is employed [28],

$$I(x, y) = \frac{P}{\pi a^2} \left[f + (1 - f) \frac{x^2 + y^2}{a^2} \right] \times \exp\left(-\frac{x^2 + y^2}{a^2}\right) \quad (2)$$

2.2.1. Governing equations

Based on a fixed-grid numerical method [6,10,18], the governing equations for continuity, momentum and energy for such laser surface melting of ceramic materials in the defined Cartesian coordinate system can be written as:

continuity:

$$\frac{\partial \rho}{\partial t} + \frac{\partial}{\partial x}(\rho u) + \frac{\partial}{\partial y}(\rho v) + \frac{\partial}{\partial z}(\rho w) = 0 \quad (3)$$

x momentum:

$$\begin{aligned} \frac{\partial}{\partial t}(\rho u) + \frac{\partial}{\partial x}(\rho uu) + \frac{\partial}{\partial y}(\rho uv) + \frac{\partial}{\partial z}(\rho uw) \\ = -\frac{\partial p}{\partial x} + \frac{\partial}{\partial x}\left(\mu \frac{\partial u}{\partial x}\right) + \frac{\partial}{\partial y}\left(\mu \frac{\partial u}{\partial y}\right) + \frac{\partial}{\partial z}\left(\mu \frac{\partial u}{\partial z}\right) \\ - \frac{\mu}{K}(u - U) \end{aligned} \quad (4)$$

y momentum:

$$\begin{aligned} \frac{\partial}{\partial t}(\rho v) + \frac{\partial}{\partial x}(\rho vu) + \frac{\partial}{\partial y}(\rho vv) + \frac{\partial}{\partial z}(\rho vw) \\ = -\frac{\partial p}{\partial y} + \frac{\partial}{\partial x}\left(\mu \frac{\partial v}{\partial x}\right) + \frac{\partial}{\partial y}\left(\mu \frac{\partial v}{\partial y}\right) + \frac{\partial}{\partial z}\left(\mu \frac{\partial v}{\partial z}\right) - \frac{\mu}{K}v \end{aligned} \quad (5)$$

z momentum:

$$\begin{aligned} \frac{\partial}{\partial t}(\rho w) + \frac{\partial}{\partial x}(\rho wu) + \frac{\partial}{\partial y}(\rho wv) + \frac{\partial}{\partial z}(\rho ww) \\ = -\frac{\partial p}{\partial z} + \frac{\partial}{\partial x}\left(\mu \frac{\partial w}{\partial x}\right) + \frac{\partial}{\partial y}\left(\mu \frac{\partial w}{\partial y}\right) + \frac{\partial}{\partial z}\left(\mu \frac{\partial w}{\partial z}\right) \\ - \frac{\mu}{K}w + \rho g \beta (T - T_{ref}) \end{aligned} \quad (6)$$

energy:

$$\begin{aligned} \frac{\partial}{\partial t}(\rho T) + \frac{\partial}{\partial x}(\rho u T) + \frac{\partial}{\partial y}(\rho v T) + \frac{\partial}{\partial z}(\rho w T) \\ = \frac{\partial}{\partial x}\left(\frac{k}{c} \frac{\partial T}{\partial x}\right) + \frac{\partial}{\partial y}\left(\frac{k}{c} \frac{\partial T}{\partial y}\right) + \frac{\partial}{\partial z}\left(\frac{k}{c} \frac{\partial T}{\partial z}\right) \\ + \frac{q(x, y, z)}{c} - \frac{\partial}{\partial t}\left(\frac{\rho \Delta H}{c}\right) - \frac{\partial}{\partial x}\left(\frac{\rho u \Delta H}{c}\right) \\ - \frac{\partial}{\partial y}\left(\frac{\rho v \Delta H}{c}\right) - \frac{\partial}{\partial z}\left(\frac{\rho w \Delta H}{c}\right) \end{aligned} \quad (7)$$

In the momentum equations, the permeability term, K , is related to the liquid volume fraction by the Carman–Koseny equation [12],

$$\frac{1}{K} = \frac{D(1 - f_L)^2}{f_L^3 + \delta} \quad (8)$$

where f_L is the liquid volume fraction, δ is a small number (0.001) to prevent division by zero and D is the “mushy” zone constant. The liquid volume fraction, f_L , as shown in Fig. 5, is defined as:

$$f_L = \begin{cases} 0, & T \leq T_{\text{sol}} \\ f_L(T), & T_{\text{sol}} < T < T_{\text{liq}} \\ 1, & T \geq T_{\text{liq}} \end{cases} \quad (9)$$

where T_{sol} and T_{liq} are the solidus and liquidus temperatures respectively, and $f_L(T)$ is derived directly from the temperature–composition relationship in the phase diagram (Fig. 2) using a piecewise linear interpolation method. A small temperature interval, $\Delta T = 1 \text{ K}$, has been employed to describe the eutectic melting process. Smaller ΔT values are applicable, but the numerical solution is not appreciably influenced and becomes more costly. The “mushy” zone constant was taken as 10^{10} m^{-2} .

The energy equation is expressed directly in terms of temperature, where the latent heat of fusion is calculated from the temperature–composition relationship in the phase diagram and accounted for as an additional heating source.

2.2.2. Boundary conditions

By introducing the permeability term and source-based method, the above governing equations, Eqs. (3)–(7) are unique for both liquid and solid phases; therefore, it is not necessary to track the melt/solid inter-

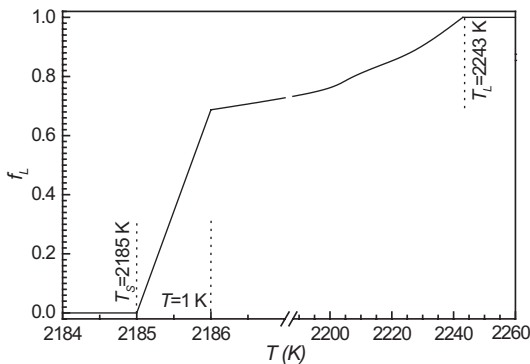


Fig. 5. The liquid volume fraction defined as a function of temperature and derived from the temperature–composition relationship in the used phase diagram, using a piecewise linear interpolation method.

face and specify a boundary condition at that location. Except for the melt/vapour interface, at the top, bottom, front and back sides of the workpiece, the thermal boundaries are all described by [6]

$$k \frac{\partial T(x, y, z)}{\partial n} = -q(x, y, z)dn + h_C(T - T_\infty) \quad (10)$$

where h_C is a combined transfer coefficient for the radiative and convective boundary conditions, and can be calculated from the relationship given by Goldak [6]:

$$h_C = 24.1 \times 10^{-4} \varepsilon T^{1.61} \quad (11)$$

The right boundary is maintained at its initial temperature:

$$T(x_{\text{right}}, y, z) = T_0 \quad (12)$$

and, at the left side, the adiabatic wall boundary condition is adopted:

$$k \left(\frac{\partial T}{\partial x} \right)_{\text{left}} = 0 \quad (13)$$

In addition, once vaporization occurs, the temperatures at the melt/vapour interface are fixed as either the vaporization temperature at standard state, $T_{\text{vap},0}$, or those values are dependent on the absorbed laser intensities, I_{abs} , if they are higher than $T_{\text{vap},0}$. Here, the equation derived by Ganesh et al. [21] from gas dynamics, by assuming that the vapour behaves as an ideal gas and follows the Clausius/Clapeyron equation, is employed to determine the temperatures higher than $T_{\text{vap},0}$ at the melt/vapour interface:

$$\begin{aligned} \frac{\kappa + 1}{L_v \kappa} \sqrt{\kappa R T} \left(I_{\text{abs}} + k \frac{\partial T}{\partial n} \right) \\ = P_{\text{vap},0} \exp \left[\frac{L_v}{R} \left(\frac{1}{T_{\text{vap},0}} - \frac{1}{T} \right) \right] \end{aligned} \quad (14)$$

As the laser beam intensities used for laser surface melting are lower than those used for laser drilling in Ref. [21], the following approximation is applied in Eq. (14).

$$\frac{\partial T}{\partial n} = \frac{I_{\text{abs}}}{k} \quad (15)$$

For the fluid flow, at the assumed flat top surface of the melt pool:

$$w_{\text{top}} = 0 \quad (16)$$

Also, the surface tension or Marangoni-driven flow, from the balance between shear force and surface tension, at the top surface of the melt pool, is described by

$$\tau_{xz} = -\mu \left(\frac{\partial u}{\partial z} \right)_{\text{top}} = \sigma_T \left(\frac{\partial T}{\partial x} \right)_{\text{top}} \quad (17a)$$

$$\tau_{yz} = -\mu \left(\frac{\partial v}{\partial z} \right)_{\text{top}} = \sigma_T \left(\frac{\partial T}{\partial y} \right)_{\text{top}} \quad (17b)$$

Eqs. (1) to (17) formulate the mathematical model completely for the present convection–diffusion phase-change process during laser surface melting of ceramic materials using a fixed-grid numerical method [6,10].

3. Numerical procedures

3.1. Grids

Making use of the symmetry to x – z plane, only half the workpiece is considered in the calculation. In order to improve the accuracy of the calculation, variable spacing for the grid system has been utilized. In the vertical direction, a grid size of 0.02 mm was chosen close to the top surface in order to provide sufficient resolution to capture the flow details inside the surface tension-driven boundary layer. A boundary layer thickness of 0.1–0.2 mm was estimated for the present simulation cases, using a scaling analysis developed in a previous paper [30]. Below this boundary layer, at least 10 grids must be included to the bottom of the melt pool. In the horizontal planes, 40×15 grids were uniformly distributed within the melt pool. The position and dimensions of the melt pool were estimated approximately from the semi-analytical heat conduction model developed in another paper [8]. Outside the melt pool, in the solid region, coarser grids were used. Overall, a $60 \times 30 \times 30$ rectangular grid system was used to discretize the calculated domain of $80 \text{ mm} \times 40 \text{ mm} \times 15 \text{ mm}$.

3.2. Numerical scheme and solution

The governing equations and boundary conditions formulated in Eqs. (1) to (17) were discretized and solved using the SIMPLER algorithm outlined by Patankar [18]. The energy equation, Eq. (7), can be discretized as

$$a_P T_P = a_E T_E + a_W T_W + a_N T_N + a_S T_S + a_T T_T + a_B T_B + b \quad (18)$$

where the subscripts indicate the appropriate nodal values, the ‘ a ’ terms are coefficients dependent on the diffusion, convective and the latent heat of fusion fluxes into the P th control volume, and the parameter, b , includes the terms associated with the evaluation of temperature at the previous time step, the volumetric laser heating source and the latent heat of fusion. The connection process for the convection and diffusion terms in the coefficients was handled using the power-law scheme [18]. Compared with the discretization equation given in Ref. [18], a major modification in the present Eq. (18) was the incorporation of terms related to the latent heat of fusion, which are fully described in the Appendix A.

The momentum equations Eqs. (4)–(6) can be discretized into equations similar to Eq. (18). An important difference is that the grids used are “staggered” over the temperature grids, where the latter grid points are located midway between the former grid points. The ‘ a ’ coefficients depend on the viscous diffusion and convective fluxes into the p th control volume, and the parameter b includes the terms associated with evaluation of the velocities at the previous time step and the permeability term. In addition, the momentum source due to surface tension in the x direction and the moving workpiece are added to parameter b in the x -momentum equation. The momentum source due to surface tension in the y direction is added to parameter b in the y -momentum equation, and the momentum source due to buoyancy force is added to parameter b in the z -momentum equation. More details of the staggered grids and the discretization momentum equations are given in Refs. [10,18].

The governing nonstationary equations were used as a means to reach steady state. The simulation was carried out from an initial temperature of 293 K. The time steps were adjusted during the various stages in the melting process. During the solid conduction stage, a large time step, 0.1 s, was used until melting began. Then a small time step, 0.0005 s, was chosen for the initial stage in melt pool development. As expected, significant numerical oscillations in the solved variables for the nodes around the solid/melt interfaces were still observed. In the previous numerical methodologies applied to “mushy” region phase-change processes, the energy equation was expressed in terms of the sensible enthalpy and the poor convergence of the energy equation was avoided by updating the sensible enthalpy with under-relaxed liquid fractions [10]. In the present investigation, the energy equation was directly written in terms of temperature. The permeability term in the momentum equations, K , dependent on temperature, was under-relaxed. For the following two simulation cases, a relaxation factor of 0.9 for updating the permeability term, in conjunction with a relaxation factor of 0.5 for updating the velocities, has been found to be successful in achieving calculation convergence. After the melt pool was sufficiently developed, time steps could be increased properly, up to a maximum of 0.05 s. Within each time step, calculation convergence was verified after the relative residues of all the temperature and velocity values were less than 10^{-4} . The calculation was terminated at a total time of 10 s that was sufficient to reach steady state.

3.3. Simulation cases

As the numerical procedure for the convection–diffusion phase change process, involving both the latent heat of fusion and fluid flow, still needs considerable computer power and long computing time, only two cases, i.e.

Table 2
Laser processing parameters and corresponding codes for the two simulation cases

Case code	P (W)	d (mm)	U (mm/s)
C1	1000	10	10
C2	1000	10	5

two sets of laser process parameters used to treat the refractory ceramic, have been simulated. These sets and the corresponding codes are listed in Table 2. For purposes of comparison, the two cases have also been simulated using the corresponding numerical models for pure heat conduction and heat conduction that incorporates latent heat of fusion, by deleting the related terms in the energy equation and omitting the momentum equations.

All calculations were executed using self-written codes of the MATLAB R12 (The Mathworks, Inc.) on a PC computer with Intel[R] Pentium[R]4 CPU 2.40GHz processor and 512.0MB RAM. The run time depended on the laser process parameters and the corresponding model. For the two models that did not consider fluid flow, the running times were less than 50h. For the model that consider both latent heat of fusion and fluid flow, case C1 required the order of one week, while case C2 required the order of one month.

4. Results

4.1. Temperature field

All data presented here are for a time of 10s. Figs. 6 and 7 present the temperature contours on the $z = 0$ and $y = 0$ planes of the workpiece for the two cases simulated using the three models. These contours are similar to those obtained from a previous analytical heat conduction model [8]. It has been demonstrated that, due to motion of the workpiece relative to the laser beam, causing advection heat flow to occur in the moving direction, the peak temperatures at the workpiece surface were near the trailing edge of the laser beam rather than at the beam centre [8,31]. The present models were mainly concerned with the effects of latent heat of fusion and fluid flow on the temperature distribution. It is observed that, the effect of the latent heat of fusion is more significant than the effect of fluid flow, especially on the temperature distribution within the melt pool. Owing to the convective terms in the latent heat of fusion, a considerable amount of heat flows from the molten centre towards the trailing domain of the laser beam, leading to a decreased peak temperature and a relatively more uniformly distributed temperature on the workpiece surface. The weaker effect of fluid flow arises from the following two opposing trends. On the one hand, fluid

flow causes the fluid at higher temperature to flow from the molten centre outwards towards the solid–liquid interface, tending to increase the size of the melt pool; on the other hand, fluid flow consumes a certain amount of laser energy, resulting in a smaller melt pool. Away from the surface, the temperature fields calculated using the three models are almost identical.

From the results of the two simulation cases, the three models all predict that a slower moving velocity of the workpiece would lead to larger temperature gradients in the direction of movement of the workpiece, but lower temperature gradients in the directions vertical to the movement of the workpiece within the solid domain where the temperature is lower than the melting point, in addition to a high peak temperature on the molten surface. This is consistent with a previous analytical heat conduction model [8]. However, the present comparison further indicates that, for a slower moving velocity of the workpiece, the effect of latent heat of fusion on the temperature distribution is relatively less significant, and the effect of fluid flow on the temperature distribution becomes relatively more significant.

4.2. Velocity field

Figs. 8 and 9 depict the velocity vectors on the three planes, through the hottest centre and vertical to one another, for the two cases, that were simulated using the model for the convection–diffusion phase change process involving both latent heat of fusion and fluid flow. It should be noted that the x components of the velocity vectors have been subtracted from the moving velocity of the workpiece. Despite the fact that a volumetric heating source has been used to model the incidental laser energy, the present flow patterns are similar to those observed during laser melting of metallic materials, modelled using a surface heating source, for negative temperature coefficients of surface tension [6,32]. This is not surprising because the present fluid flow is still driven by surface tension or the Marangoni force and the thermal buoyancy force. The flow is directed radially outwards from the hottest centre to the external field of the melt pool. At the edge of the pool, the direction of flow is downwards, along the melt/solid interface to the bottom of the melt pool, and, from there, upwards, thereby closing the circle while preserving the mass. However, more asymmetry flow patterns have been observed for the present results. This can be readily attributed to the fact that the latent heat of fusion for the present refractory ceramic is obviously larger than those for the metallic materials, where heat is absorbed at the front of the melting interface, but liberated at the trailing solidifying interface, due to motion of the workpiece relative to the laser beam; thus results in more asymmetrical temperature gradients and surface tension forces between the front and trailing sides of the melt pool.

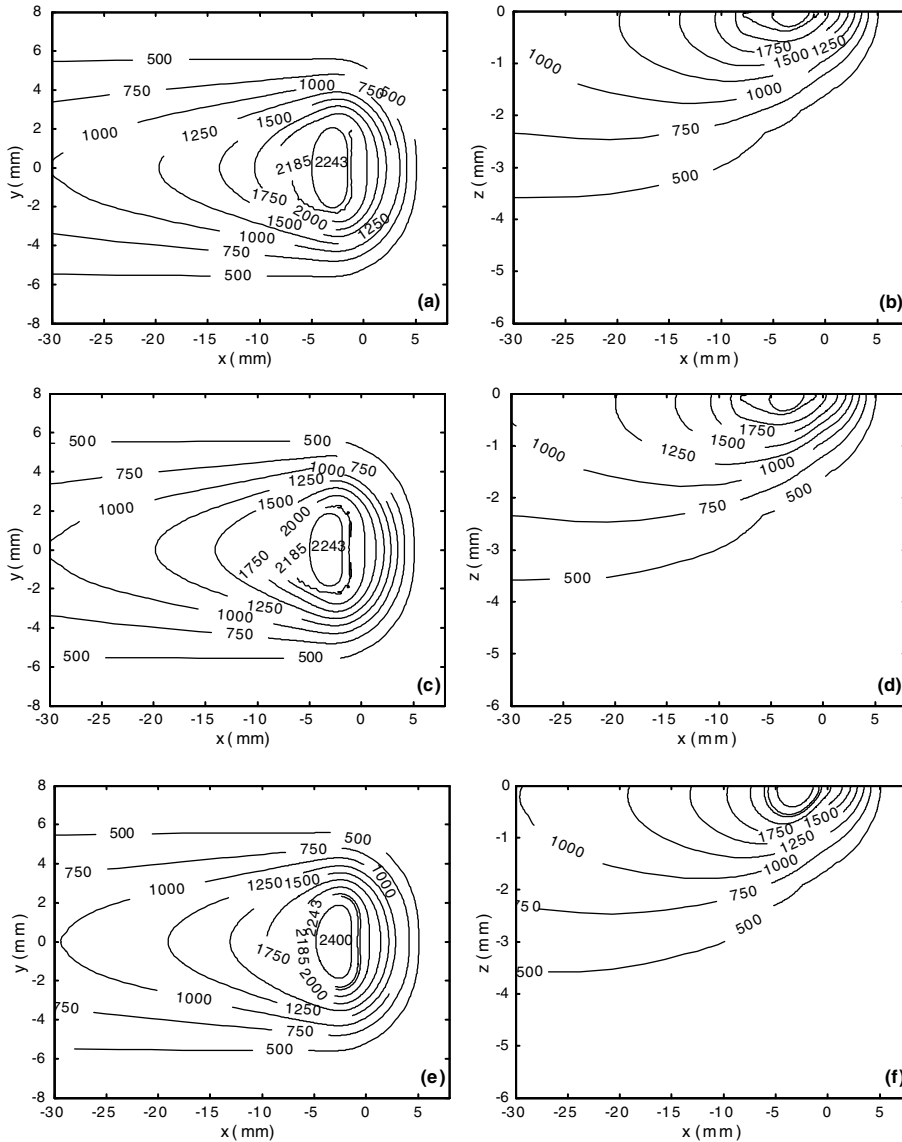


Fig. 6. The temperature contours for the planes of $z = 0$ and $y = 0$ for case C1 simulated using the three models: (a), (b) the model involving both latent heat of fusion and fluid flow; (c), (d) the model for heat conduction incorporating latent of fusion and (e), (f) the model for pure heat conduction.

Based on Figs. 8 and 9, it is easy to understand why, for a smaller moving velocity of the workpiece, and provided that the other laser process parameters are identical, the effect of fluid flow on the temperature distribution becomes relatively more significant. This is due to the larger flow velocities, associated with a higher peak temperature within the melt pool; these cause a greater amount of heat to flow from the hotter region to the colder region, resulting in the shape of the melt pool and temperature distribution being modified more significantly.

4.3. Shape of the melt pool

Figs. 10 and 11 illustrate the contours of depth of the melt pool projected onto the workpiece surface for the two cases simulated using the three models. Note that the x - y scales of Figs. 10 and 11 are much smaller than those of Figs. 6 and 7. Consistent with the corresponding temperature distribution, the effect of latent heat of fusion on the shape of the melt pool is much more significant than the effect of fluid flow. As a result of the absorption and liberation of latent heat of fusion at

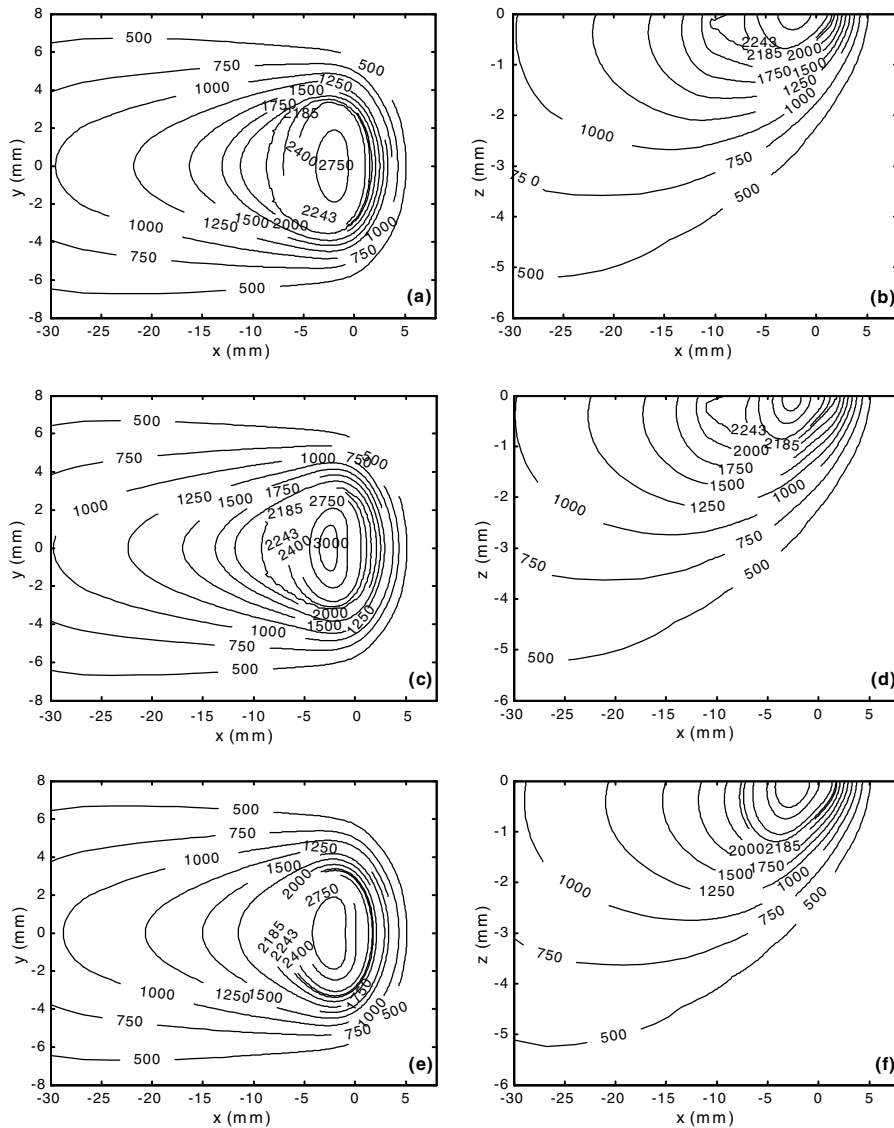


Fig. 7. The temperature contours for the planes of $z = 0$ and $y = 0$ for case C2 simulated using the three models: (a), (b) the model involving both latent heat of fusion and fluid flow; (c), (d) the model for heat conduction incorporating latent of fusion and (e), (f) the model for pure heat conduction.

the melting and solidifying interfaces, the simulated melt pool is obviously longer in the direction of movement of the workpiece, shallower in the direction of laser incidence, but slightly narrower in the direction vertical to both the direction of movement of the workpiece and the direction of laser incidence.

Fig. 12 compares further the predicted cross-sectional profiles for the melt/solid interfaces with the experimental results measured using an image analysis method for the two cases. The related experimental procedure and image analysis method have been described in detail in a previous publication by the authors [8], and, thus,

are not repeated here. The experimental and predicted melt depths, half-widths and cross-sectional areas determined from this figure are listed in Table 3. In addition, the melt volumes predicted from the three models are also listed in Table 3 although they cannot be experimentally measured. From Fig. 12 and Table 3, it can be seen that the profiles predicted from the model involving pure heat conduction are apparently larger than the experimentally measured profiles for both cases. The profiles predicted from the model for heat conduction that involves latent heat of fusion are in good agreement with the measured profiles. The profiles

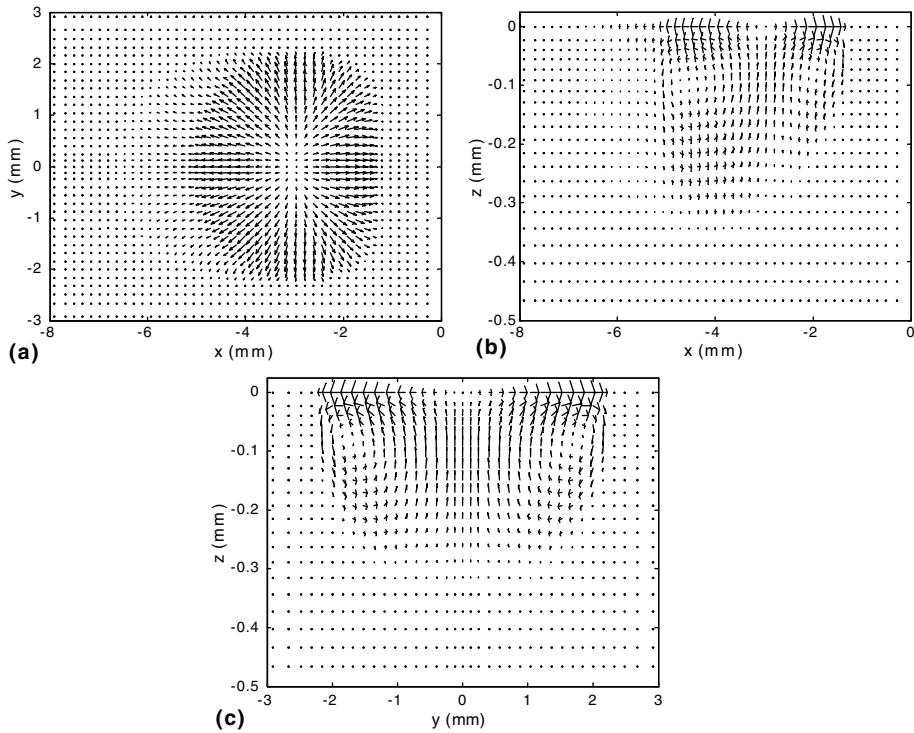


Fig. 8. The velocity vectors simulated using the model involving both latent heat of fusion and fluid flow for case C1 on planes of (a) $z = 0$, maximum vector = 0.045 m/s; (b) $y = 0$, maximum vector = 0.045 m/s and (c) $x = -3.1$, maximum vector = 0.038 m/s.

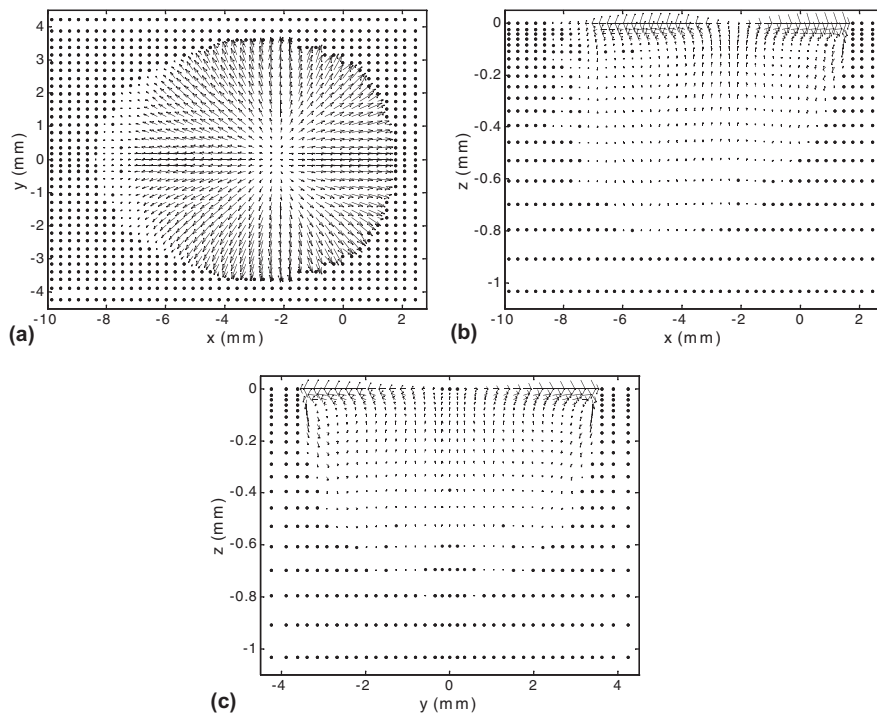


Fig. 9. The velocity vectors simulated using the model involving both latent heat of fusion and fluid flow for case C2 on planes of (a) $z = 0$, maximum vector = 0.098 m/s; (b) $y = 0$, maximum vector = 0.073 m/s and (c) $x = -2.4$, maximum vector = 0.092 m/s.

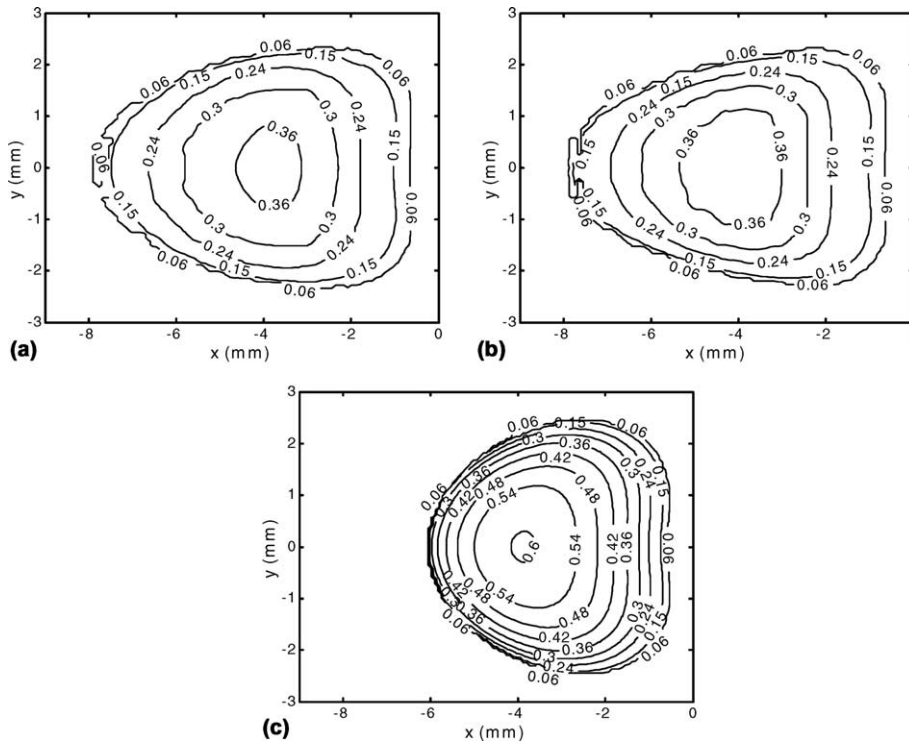


Fig. 10. The contours for depth of the melt pool projected on the workpiece surface for case C1, simulated using the three models: (a) the model involving both latent heat of fusion and fluid flow; (b) the model for heat conduction incorporating latent of fusion and (c) the model for pure heat conduction.

predicted from the model that involves both latent heat of fusion and fluid flow of the melt pool are in closer agreement with the measured profiles. Compared with the previous analytical model of heat conduction [8], the present numerical model for pure heat conduction has somewhat less precisely predicted the cross-sectional profiles. This may be related to the different thermophysical properties of the workpiece material, used in the two models. In the previous analytical model, constant thermophysical properties were used. In the present numerical model, both constant and temperature-dependent properties, as shown in Table 1 and Fig. 3, have been used. However, once the present numerical model for heat conduction incorporates the latent heat of fusion, the prediction accuracy for the cross-sectional profiles was much improved, and good agreement between the predicted and experimental profiles was observed. Theoretically, the model that involves both latent heat of fusion and fluid flow of the melt pool is more reasonable for describing the physical process that occurs during laser melting of the treated material. Since high prediction accuracy for the cross-sectional profiles of the melt/solid interfaces has been observed for the model for heat conduction that incorporates latent heat of fusion, and only slightly further improved prediction accuracy has been achieved for the model

that involves both latent heat of fusion and fluid flow, it is justified to conclude that the absorption and liberation of the latent heat of fusion at the melting and solidifying interfaces are more significant than fluid flow in influencing the final shape and size of the melt pool, for the present two simulation cases.

5. Discussion

The present modelling procedure has dealt with a combined situation, where a phase change involving melting/solidifying at a eutectic composition takes place at both a distinct temperature and over a temperature range. During the numerical procedure, both the latent heat of fusion and liquid volume fraction were updated according to a realistic binary phase diagram containing a eutectic composition, using a piecewise linear interpolation method. Compared with previous numerical models for isothermal phase-change processes that occur at a distinct temperature [13,14], the present model has retained the last three terms in the energy equation during numerical simulation. Compared with previous numerical models for mushy region phase-change processes that occur over a temperature range, in which the energy equation was written in terms of the sensible enthalpy

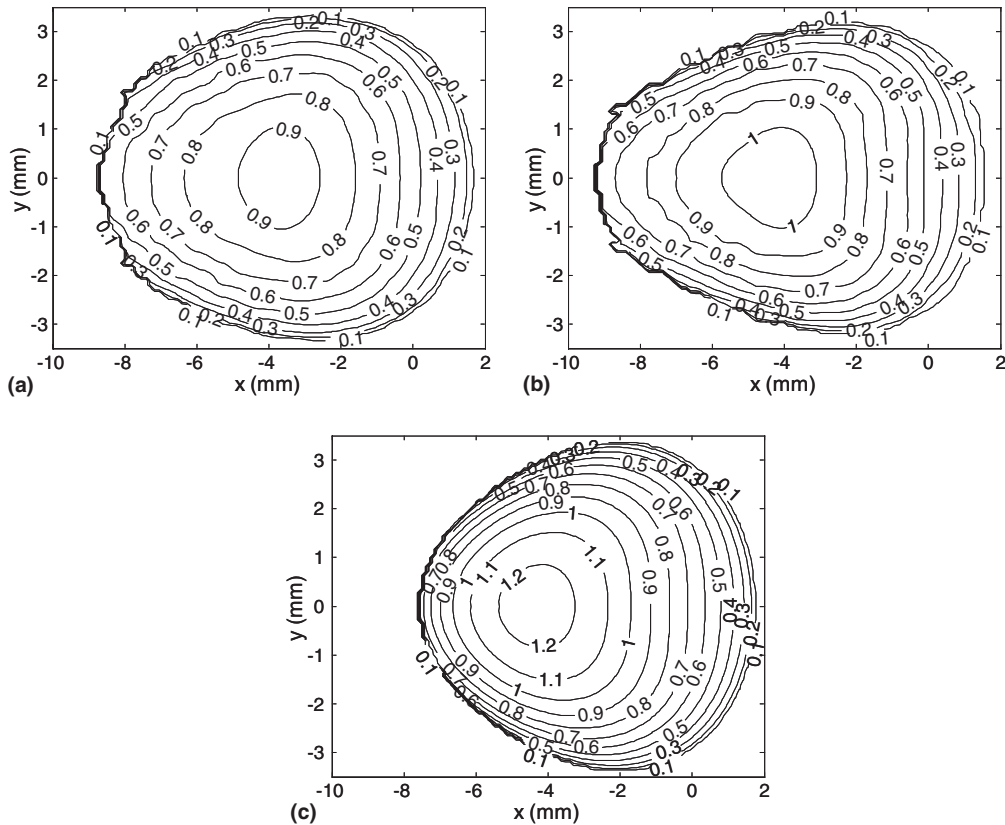


Fig. 11. The contours for depth of the melt pool projected on the workpiece surface for case C2, simulated using the three models: (a) the model involving both latent heat of fusion and fluid flow; (b) the model for heat conduction incorporating latent of fusion and (c) the model for pure heat conduction.

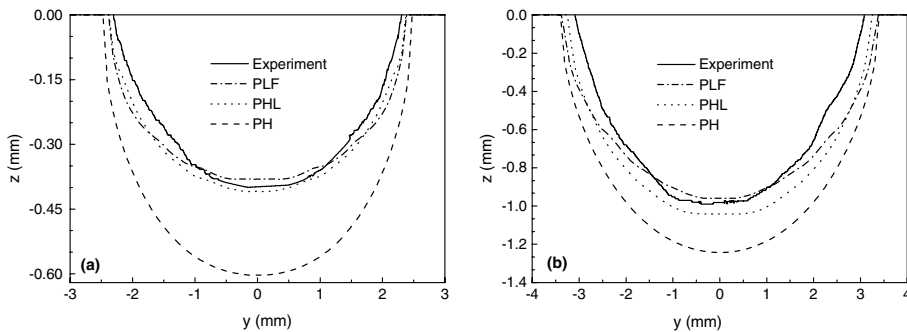


Fig. 12. The cross-sectional profiles of the melt/solid interfaces predicted from the three models: the model involving both latent heat of fusion and fluid flow, PLF; the model for heat conduction incorporating latent of fusion, PHL and the model for pure heat conduction, PH, compared with those measured using image analysis method for (a) case C1 and (b) case C2.

[10,12], the present model has used the energy equation expressed directly in terms of temperature. Such an energy equation is obviously more convenient for some cases, for example, multi-layered composite workpiece materials. This is because it is the temperature, not the

enthalpy, that should be continuous across the interfaces between different layers.

To the authors' knowledge, no previous model has been developed for such a convection–diffusion phase-change process. Thus, no existing study is available in

Table 3
Comparison of the experimental and predicted melt depths, half-widths and cross-sectional areas

Case code	C1	C2
Experimental results		
W_{exp} (mm)	2.30 (0.07)	3.09 (0.09)
D_{exp} (mm)	0.40 (0.05)	0.99 (0.13)
S_{exp} (mm ²)	1.36 (0.14)	4.38 (0.31)
Predictions from model considering both latent heat of fusion and fluid flow		
W_{LF} (mm)	2.34	3.43
D_{LF} (mm)	0.38	0.96
S_{LF} (mm ²)	1.42	4.96
V_{LF} (mm ³)	6.76	35.69
Predictions from model of heat conduction incorporating latent heat of fusion		
W_{HL} (mm)	2.33	3.19
D_{HL} (mm)	0.41	1.04
S_{HL} (mm ²)	1.50	5.24
V_{HL} (mm ³)	6.89	36.11
Predictions from model of pure heat conduction		
W_{H} (mm)	2.46	3.38
D_{H} (mm)	0.60	1.24
S_{H} (mm ²)	2.37	6.48
V_{H} (mm ³)	8.88	38.91

Note that the experimental data in parentheses stand for the differences in lower or upper bounds from the average values.

the literature to validate the present modelling. Nonetheless, an analytical model of heat conduction and a scaling analysis for momentum and heat transport in the laser-induced melt pool of ceramic materials previously developed in Refs. [8,30] can be employed to evaluate the present numerical results. The temperature fields simulated using the present models were similar to those calculated from the previous analytical model of heat conduction [8]. The difference in temperature distributions calculated from the different models was physically reasonable as aforementioned. According to the scaling analysis for momentum and heat transport in the laser-induced melt pool of ceramic materials, outlined in a previous paper [30], the effect of workpiece traverse velocity, for the laser process parameters in the present cases, C1 and C2, on the reference velocity and velocity boundary layer thickness is negligible: the reference velocities for fluid flow in the x , y and z directions were respectively 0.081, 0.081 and 0.013 m/s, and the velocity boundary layer thickness at the melt surface was about 0.2 mm. With regard to the fact that a scaling analysis is mainly used to predict the orders of magnitude values of these quantities, they are in excellent agreement with the present numerical results, as shown

in Figs. 8 and 9. The thermal diffusivity of the present refractory ceramic, one order of magnitude lower than those of the metallic materials used in Refs. [12,33], tends to lead to a relatively higher thermal gradient and, thus, a higher surface tension-driven flow velocity; on the other hand, the volumetric heating resource used in the present model would result in a significant decrease in the thermal gradient and the surface tension-driven flow velocity when compared with a corresponding surface heating source. Thus, it is also reasonable that the flow velocities simulated for the present melt pools are somewhat lower than those simulated for the melt pools of metallic materials produced by laser or other high energy density beams [6,12,33]. From the above analysis and discussion, it can be concluded that, theoretically, the present numerical results for the temperature and velocity distributions should be reliable.

For a fixed-grid source-based numerical model, the “mushy” zone constant, D , depends on the morphology of the “mushy” region and is usually determined by experiment [6,10]. In the present work, D has been taken as a large value: 10^{10} m^{-2} . This is because, on the one hand, such a large value was used to confirm the calculation convergence of the present numerical procedure. Convergence difficulty is often encountered in simulations where a large value of the “mushy” zone constant is used [10]. On the other hand, the experimental results indicated that the widths of the “mushy” zones varied from less than 0.1 mm to 0.5 mm, due to the porous and heterogeneous nature in the structure of the treated refractory ceramic [8]. The present simulation results (Figs. 6–9) are well within the range of experimental widths of the “mushy” zones.

Also, since cracks, open pores and corundum aggregates, from less than 1 mm to 5 mm in size, were visible on the treated surface of the refractory ceramic [34], apparently, temperature and velocity varied significantly around these features. These parameters were not measured during laser melting. Therefore, only the final profiles of the melt/solid interfaces have been used to assess experimentally the reliability of the present numerical models. As shown in Fig. 12, the best prediction for the profiles was achieved from the model that involved both latent heat of fusion and fluid flow. Some discrepancies were still observed between the predicted and experimental profiles for the melt/solid interfaces. The main reason may be due to deviations in the modelled mix of Gaussian and Doughnut modes from the actual mix in laser energy distribution [8]. Another reason may be attributed to the complex structure and composition of the refractory ceramic [3,34], making it difficult to model its thermophysical properties accurately. In particular, the dynamic viscosity and temperature coefficient of surface tension for liquid alumina have been used for the present simulation, due to lack of accurate

high-temperature data for the treated refractory ceramic. For metallic materials, it was found that the temperature coefficients for surface tension vary with temperature and concentrations of the various surface-active elements, such as sulfur, oxygen and manganese [14,35]. It can be expected that several minor chemical constituents, such as Cr₂O₃, P₂O₃, Fe₂O₃, TiO₂, MgO, Na₂O, CaO and K₂O, present in the treated refractory ceramic [3], influence the dynamic viscosity and temperature coefficient of surface tension. If the laser energy distribution and these effects can be more accurately determined, the prediction accuracy should be further improved.

6. Conclusions

A three-dimensional numerical modelling for the convection–diffusion phase change process during laser melting of ceramic materials has been studied, using a fixed-grid source-based method. The model used the energy equation written directly in terms of temperature. During the numerical procedure, the latent heat of fusion, accounted for as an additional heating source in the energy equation, was updated according to a realistic binary phase diagram that included a eutectic composition, using a piecewise linear interpolation method. The permeability term in the momentum equations, associated with the nodal temperatures, was under-relaxed to avoid poor convergence.

For the two simulation cases, it was found that the absorption and liberation of latent heat of fusion at the melting and solidifying interfaces were more significant than fluid flow in influencing the temperature distribution and the final shape and size of the laser-induced melt pool. Theoretical analysis indicated that the temperature and velocity fields simulated using the presently developed numerical model involving both latent heat of fusion and fluid flow should be reliable.

The cross-sectional profiles for the melt/solid interfaces predicted from the presently developed numerical model were in excellent agreement with experimental results. Slight discrepancies observed between the predicted and experimental melt/solid interfaces may be attributed to inaccuracies in the laser energy distribution and the thermophysical properties of the refractory ceramic in the model.

Acknowledgments

This research was funded by the Engineering and Physical Science Research Council (Grant Ref. GR/N08124) in collaboration with Cleanaway Ltd, BNFL, Morgan Materials Technology Ltd, ICI and Plasma Thermal Coatings Ltd.

Appendix A. Numerical treatment of latent heat of fusion

The latent heat of fusion, accounted for as an additional heating source, in Eq. (7), can be assumed to consist of two parts, a transient term and a convective term. The transient term was discretized as the following expression

$$\begin{aligned} & \frac{\partial}{\partial t} \left(\frac{\rho \Delta H}{c} \right) \\ &= \frac{1}{\Delta t} \left(\frac{\rho_P \Delta H_P}{c_P} - \frac{\rho_P^0 \Delta H_P^0}{c_P} \right) \\ &= \begin{cases} 0 & T_P^0 < T_{sol}, T_P < T_{sol} \\ & \text{or } T_P^0 > T_{liq}, T_P > T_{liq} \\ \frac{\rho_P c_P^H}{\Delta t c_P} (T_P - T_S) - \frac{\rho_P^0 \Delta H_P^0}{\Delta t c_P} & \text{otherwise} \end{cases} \end{aligned} \tag{A.1}$$

The convective part of the latent heat source was treated via an upwinding discretization. Its contribution to the source term may be written in the following form:

$$\begin{aligned} & \frac{\partial}{\partial x} \left(\frac{\rho u \Delta H}{c} \right) + \frac{\partial}{\partial y} \left(\frac{\rho v \Delta H}{c} \right) + \frac{\partial}{\partial z} \left(\frac{\rho w \Delta H}{c} \right) \\ &= \Delta H_{inflow} - \Delta H_{outflow} \end{aligned} \tag{A.2}$$

with

$$\begin{aligned} \Delta H_{inflow} = & |[F_w, 0]| T_W - |[-F_w, 0]| T_P \\ & + |[F_s, 0]| T_S - |[-F_s, 0]| T_P + |[F_b, 0]| T_B \\ & - |[-F_b, 0]| T_P - (|[F_w, 0]| - |[-F_w, 0]| \\ & + |[F_s, 0]| - |[-F_s, 0]| + |[F_b, 0]| - |[-F_b, 0]|) T_{sol} \end{aligned} \tag{A.3a}$$

$$\begin{aligned} \Delta H_{outflow} = & |[F_e, 0]| T_P - |[-F_e, 0]| T_E \\ & + |[F_n, 0]| T_P - |[-F_n, 0]| T_N + |[F_t, 0]| T_P \\ & - |[-F_t, 0]| T_T - (|[F_e, 0]| - |[-F_e, 0]| \\ & + |[F_n, 0]| - |[-F_n, 0]| \\ & + |[F_t, 0]| - |[-F_t, 0]|) T_{sol} \end{aligned} \tag{A.3b}$$

where $[A, B]$ means the maximum of A and B and

$$\begin{aligned} F_w &= \frac{(\rho u)_w}{\Delta x c_w} c_w^H, & F_e &= \frac{(\rho u)_e}{\Delta x c_e} c_e^H \\ F_s &= \frac{(\rho u)_s}{\Delta x c_s} c_s^H, & F_n &= \frac{(\rho u)_n}{\Delta x c_n} c_n^H \\ F_b &= \frac{(\rho u)_b}{\Delta x c_b} c_b^H, & F_t &= \frac{(\rho u)_t}{\Delta x c_t} c_t^H \end{aligned} \tag{A.4}$$

were evaluated at the cell faces of the P th control volume. In essence, the formulation of the convective part of the latent heat source states that the convective loses or gains in latent heat are governed by the direction of the flow field. Such a discretization formulation is similar to the upwind differencing scheme used by Voller and

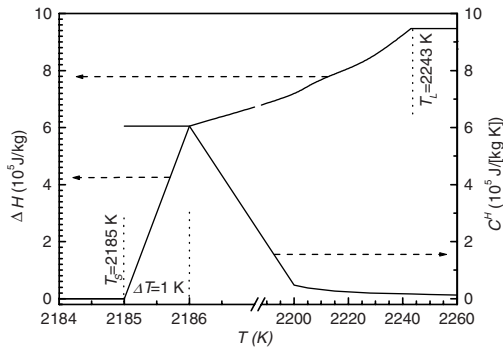


Fig. 13. The latent heat of fusion and its temperature coefficient, defined as functions of temperature and directly derived from the phase diagram in Fig. 2.

Prakash [10] to treat the convective latent heat source for convection–diffusion “mushy” region phase-change processes. However, a modification has been attained when compared to the discretization formulation directly expressed in terms of the nodal latent heats. Eq. (A.3) has been given in terms of temperature, corresponding to the discretized energy equation, Eq. (18), expressed in terms of the nodal temperatures.

During the numerical procedure, all terms in Eqs. (A.1) and (A.2) were merged to the corresponding the “*a*” coefficients or the “*b*” parameter of the discretized energy equation, Eq. (18). In Eqs. (A.1) and (A.4), the C^H terms are the temperature coefficients for latent heat of fusion. C^H and ΔH were both derived directly from the phase diagram (Fig. 2) and defined as functions of temperature, as shown in Fig. 13. Note that a small temperature interval, $\Delta T = 1$ K, has been employed to describe the eutectic melting process. During numerical iteration, both C^H and ΔH were updated according to the nodal temperatures and the corresponding curves in Fig. 13, using a piecewise linear interpolation method. If the *P*th node and its six nearest-neighbour nodes all had temperatures that were lower than the solidus temperature, or higher than the liquidus temperature of the workpiece material, the terms in the convective part of the latent heat source in Eq. (A.2) for this node may be omitted and taken as zero.

References

- [1] J. Lawrence, L. Li, J.T. Spencer, The effects of high-power diode laser radiation on the wettability, adhesion and bonding characteristics of an alumina/silica-based oxide and vitreous enamel, *Surf. Coat. Technol.* 115 (1999) 273–281.
- [2] M.J.J. Schmidt, L. Li, High power diode laser surface treatment of mullite crucible materials, *Appl. Surf. Sci.* 168 (2000) 9–12.
- [3] L. Bradley, L. Li, F.H. Stott, Flame-assisted laser surface treatment of refractory materials for crack-free densification, *Mater. Sci. Eng. A* 278 (2000) 204–212.
- [4] D. Triantafyllidis, L. Li, F.H. Stott, Surface treatment of alumina-based ceramics using combined laser sources, *Appl. Surf. Sci.* 186 (2002) 140–144.
- [5] J.F. Li, L. Li, F.H. Stott, Crystallographical analysis of surface layers of refractory ceramics formed using combined flame spray and simultaneous laser treatment method, *J. Eur. Ceram. Soc.* 24 (10–11) (2004) 3129–3138.
- [6] L.X. Yang, X.F. Peng, B.X. Wang, Numerical modeling and experimental investigation on the characteristics of molten pool during laser processing, *Int. J. Heat Mass Transfer* 44 (2001) 4465–4473.
- [7] M. Leung, Phase-change heat transfer in laser transformation hardening by moving Gaussian rectangular heat source, *J. Phys. D: Appl. Phys.* 34 (2001) 3434–3441.
- [8] J.F. Li, L. Li, F.H. Stott, Comparison of volumetric and surface heating sources in the modeling of laser melting of ceramic materials, *Int. J. Heat Mass Transfer* 47 (6–7) (2004) 1159–1174.
- [9] W.S. Kim, B.C. Sim, Study of thermal behavior and fluid flow during laser surface heating of alloys, *Numer. Heat Transfer Part A: Appl.* 31 (7) (1997) 703–723.
- [10] V.R. Voller, C. Prakash, A fixed grid numerical modeling methodology for convection–diffusion mushy region phase-change problems, *Int. J. Heat Mass Transfer* 30 (8) (1987) 1709–1719.
- [11] S. Chakraborty, P. Dutta, A generalized formulation for evaluation of latent heat functions in enthalpy-based macroscopic models for convection–diffusion phase change process, *Metall. Mater. Trans. B* 32B (2001) 562–564.
- [12] V.R. Voller, C.R. Swaminathan, General source-based method for solidification phase change, *Numer. Heat Transfer Part B* 19 (1991) 175–189.
- [13] A.D. Brent, V.R. Voller, K.J. Reid, Enthalpy-porosity technique for modelling convection–diffusion phase change: application to the melting of a pure metal, *Numer. Heat Transfer* 13 (1988) 297–318.
- [14] P. Dutta, Y. Joshi, R. Janaswamy, Thermal modeling of gas tungsten arc welding process with nonaxisymmetric boundary conditions, *Numer. Heat Transfer, Part A* 27 (1995) 499–518.
- [15] J. Lawrence, A.A. Peligard, E. Zhou, L. Li, D. Morton, Prediction of melt depth in selected architectural materials during high-power diode laser treatment, *Opt. Laser. Eng.* 35 (2001) 51–62.
- [16] A. Nisar, M.J.J. Schmidt, M.A. Sheikh, L. Li, Three-dimensional transient finite element analysis of the laser enamelling process and moving heat source and phase change considerations, *Proc. Inst. Mech. Eng. Part B: J. Eng. Manuf.* 217 (B6) (2003) 753–764.
- [17] J.F. Li, L. Li, F.H. Stott, Statistical approach for minimizing cracks in combined flame spraying and laser surface modification of refractory ceramics, *J. Eur. Ceram. Soc.* 24 (13) (2004) 3509–3520.
- [18] S.V. Patankar, *Numerical Heat Transfer and Fluid Flow*, Hemisphere, Washington, DC, 1980, pp. 133–153.
- [19] A.F.A. Hoadley, M. Rappaz, Thermal model of laser cladding by powder injection, *Metall. Trans. B* 23B (1992) 631–642.

- [20] L.M. Ernest, F. Howard, *Phase Diagrams for Ceramists*, American Ceramic Society, Columbus, Ohio, USA, 1975, Fig. 4373.
- [21] R.K. Ganesh, W.W. Bowley, R.R. Bellantone, Y. Hana, A model for laser hole drilling in metals, *J. Comput. Phys.* 125 (1996) 161–176.
- [22] E. Ryshkewitch, *Oxide ceramics: physical chemistry and technology*, Academic Press, New York, London, 1960.
- [23] CRC handbook of chemistry and physics: a ready-reference book of chemical and physical data, 76th ed, David R. Lide (editor-in-chief), H.P.R. Frederikse (associate editor), CRC Press, Boca Raton, London, 1995.
- [24] K.K. Kelley, *High temperature heat-content, heat-capacity and entropy data for the elements and inorganic compounds*, USGPO, 1960.
- [25] V. Hurevich, I. Smurov, L. Pawlowski, Theoretical study of the powder behavior of porous particles in a flame during plasma spraying, *Surf. Coat. Technol.* 151–152 (2002) 370–376.
- [26] B. Glorieux, F. Millot, J.C. Rifflet, Surface tension of liquid alumina from contactless techniques, *Int. J. Thermophys.* 23 (5) (2002) 1249–1257.
- [27] F. Millot, B. Glorieux, J.C. Rifflet, Measurements of the physico-chemical properties of liquid alumina using contactless techniques, *Progr. Astronaut. Aeronaut.* 185 (2000) 777–786.
- [28] L.G. Hector, R.B. Hetnarski, Thermal stresses in materials due to laser heating, in: R.B. Hetnarski (Ed.), *Thermal Stresses IV*, Elsevier, Amsterdam, Lausanne, New York, Oxford, Shannon, Tokyo, 1996, pp. 453–531.
- [29] J. Lawrence, E.P. Johnston, L. Li, Determination of absorption length of CO₂ and high-power diode laser radiation for ordinary Portland cement, *J. Phys., D: Appl. Phys.* 33 (2000) 945–947.
- [30] J.F. Li, L. Li, F.H. Stott, Predictions of flow velocity and velocity boundary layer thickness at surface during laser melting of ceramic materials, *J. Phys.: D. Appl. Phys.* 37 (2004) 1710–1717.
- [31] J. Cheng, A. Kar, Mathematical model for laser densification of ceramic coating, *J. Mater. Sci.* 32 (1997) 6269–6278.
- [32] H. Haferkamp, I. Burmester, C. Czerner, X-ray visualization of the transportation processes of hard particles in the melt pool of steel alloys and TiAl6V4 during laser dispersing of hard particles, in: B.L. Mordike (Ed.), *European Conference on Laser Treatment of Materials, ECLAT'98*, Werkstoff-Informationgesellschaft, 1998, pp. 111–116.
- [33] S. Chakraborty, S. Sarkar, P. Dutta, A scaling analysis of momentum and heat transport in gas tungsten arc weld pools, *Sci. Technol. Weld. Joining* 7 (2) (2002) 88–94.
- [34] J.F. Li, L. Li, F.H. Stott, Multi-layered surface coatings of refractory ceramics prepared by combined laser and flame spraying, *Surf. Coat. Technol.* 180–181 (2004) 499–504.
- [35] K.C. Mills, B.J. Keene, R.F. Brooks, A. Shirali, Marangoni effects in welding, *Philos. Trans. Roy. Soc. London, Ser. A* 356 (1998) 911–925.